Metal–Oxide Promotion Effects in Inverse Cobalt Catalysts for Selective CO_2 Methanation

Authors

Haruto Sato[1*], Yui Nakamura[2]

Affiliations

Department of Chemical System Engineering, School of Engineering, The University of Tokyo, 7-3-1 Hongo, Bunkyo-ku, Tokyo 113-8656, Japan

***Corresponding author:** HSator@u-tokyo.ac.jp

Abstract

Inverse cobalt catalysts provide unique metal–oxide boundary sites for CO_2 methanation, but the role of oxide promotion remains unclear. Herein, ZrOx-, CeOx-, and TiOx-decorated Co catalysts were synthesized and tested for CO_2 methanation at 220–360°C and atmospheric pressure. The ZrOx-modified Co catalyst showed the highest CH_4 formation rate of 7.8 mmol $gcat^{-1}$ h^{-1} at 300°C, with CO_2 conversion of 61.4% and CH_4 selectivity of 96.2%. In situ DRIFTS revealed that ZrOx promoted the formation and hydrogenation of bicarbonate and formate intermediates, while CeOx enhanced oxygen storage but favored CO formation at higher temperatures. H_2 chemisorption and XPS results showed that oxide decoration modified the electron density of surface Co and improved the resistance to oxidation. The study demonstrates that inverse oxide modification can regulate both CO_2 activation and hydrogenation pathways in cobalt-based methanation catalysts.

Keywords: CO_2 methanation; inverse cobalt catalyst; oxide promoter; methane selectivity; metal–oxide interface; formate intermediate

1. Introduction

CO_2 methanation provides a practical route for converting captured CO_2 and renewable H_2 into CH_4, which can be stored, transported, and distributed through existing natural-gas infrastructure. The reaction is thermodynamically favored at relatively low temperatures, but its kinetics are limited by the high stability of CO_2 and the multiple hydrogen-transfer steps required for complete conversion to methane. Raising the reaction temperature accelerates CO_2 activation but simultaneously promotes CO formation through the reverse water–gas shift reaction, making the control of activity and selectivity particularly important in the intermediate-temperature region. Ru-based catalysts exhibit excellent low-temperature methanation activity, whereas Ni remains the most widely investigated non-noble metal because of its lower cost and high hydrogenation ability. Co represents another attractive catalytic metal because it can efficiently dissociate H_2 and hydrogenate adsorbed carbon-containing intermediates. Its catalytic behavior, however, is highly sensitive to particle size, oxidation state, local coordination, and interaction with the surrounding

oxide phase [1,2]. This sensitivity makes the metal–oxide boundary a central structural parameter rather than a secondary support effect. Recent studies of inverse oxide/metal catalysts have further shown that catalytic behavior can originate from ensembles of structurally distinct interfacial sites, whose local geometry can affect reaction mechanism, reactivity, and deactivation [3]. Such observations provide a useful conceptual basis for CO_2 methanation, where the number, composition, and dynamic state of Co–oxide interfacial sites may determine whether adsorbed carbon species undergo complete hydrogenation to CH_4 or are released as CO.

The oxidation state of cobalt is especially important because metallic and partially oxidized Co sites may promote different reaction pathways. Metallic Co is generally associated with efficient H_2 dissociation and often favors CO-mediated methanation pathways involving CO_2 dissociation or reverse water–gas shift followed by CO hydrogenation. In contrast, partially oxidized Co species and Co–O–support configurations can enhance CO_2 adsorption and stabilize oxygen-containing intermediates such as carbonate and formate species [4,5]. The relative abundance of these sites can therefore change the dominant surface chemistry. Metal–oxide interfaces provide a way to couple the two functions: oxygen-containing sites on the oxide facilitate CO_2 adsorption and polarization, while neighboring Co sites provide activated hydrogen for sequential hydrogenation [6,7]. This cooperation must nevertheless remain balanced. If CO_2 binds too weakly, the surface concentration of reactive intermediates remains low; if the oxide stabilizes bicarbonate, carbonate, or formate too strongly, these species can accumulate as spectator intermediates and slow subsequent hydrogenation. Effective methanation therefore requires an interface that activates CO_2 without excessively stabilizing partially hydrogenated oxygenates. Among oxide promoters, ZrO_2, CeO_2, and TiO_2 offer distinctly different chemical environments for cobalt. ZrO_2 possesses tunable acid–base pairs and surface hydroxyl groups that can facilitate the formation of bicarbonate, carbonate, formate, and methoxy species. Its interaction with Co can also modify cobalt dispersion and local electron density, potentially lowering the kinetic barrier for hydrogenation of oxygen-containing intermediates [8,9]. The balance between monoclinic and tetragonal ZrO_2, surface hydroxylation, and oxygen-vacancy concentration may further influence the adsorption geometry of CO_2-derived species. CeO_2 behaves differently because of its reversible Ce^{4+}/Ce^{3+} redox couple and its ability to form oxygen vacancies under reducing atmospheres. These vacancies can improve CO_2 adsorption, interfacial oxygen transfer, and electronic communication with adjacent Co particles [10]. Excessive reduction, however, may alter the relative contribution of methanation and reverse water–gas shift pathways, especially at elevated temperature. TiO_2 typically forms stronger metal–support interactions with Co and may stabilize partially oxidized cobalt or Co–O–Ti interfacial configurations [11,12]. Such interactions can promote CO_2 adsorption and alter intermediate binding, although excessive TiO_x migration or coverage can mask metallic Co sites required for H_2 activation and complete hydrogenation. The catalytic effects of these three oxides therefore arise from different combinations of acid–base chemistry, redox behavior, oxygen-vacancy

formation, and metal–support interaction. The architecture of the catalyst provides another level of control over these interfacial effects. In conventional supported catalysts, Co nanoparticles are dispersed on a continuous oxide support, and only the perimeter of each particle directly participates in metal–oxide interfacial chemistry. In an inverse configuration, nanoscale oxide domains are deposited on a larger Co surface. This geometry can increase the density of exposed oxide–metal boundaries while allowing the amount and spatial distribution of oxide coverage to be adjusted independently from the bulk metal phase. Such an arrangement is particularly useful for separating the role of the interface from changes in total Co loading. Studies of inverse oxide/metal systems have shown that nanoscale oxide decoration can modify CO_2 adsorption, charge redistribution, intermediate stabilization, resistance to metal sintering, and product selectivity [13,14]. Importantly, inverse structures may also generate multiple interfacial motifs rather than a single uniform active site. Small oxide clusters, partially reduced domains, oxygen-deficient boundaries, and isolated metal–oxygen linkages can coexist under reaction conditions. Their relative populations may change continuously with H_2/CO_2 ratio and temperature. The catalytic function of an inverse interface should therefore be evaluated as a dynamic ensemble of sites rather than as a static structural feature identified only before reaction. Despite increasing interest in Co-based CO_2 methanation, direct comparisons of different oxide modifiers remain difficult. Reported catalysts frequently vary in Co loading, particle size, oxide fraction, preparation method, reduction temperature, reaction pressure, H_2/CO_2 ratio, and gas hourly space velocity. Changes in apparent activity may therefore originate from differences in exposed metallic Co area rather than from the intrinsic promotion effect of the oxide. Many studies also rely primarily on CO_2 conversion and CH_4 selectivity, while normalized reaction rates, hydrogen chemisorption data, and extended stability measurements are less consistently reported. This limits quantitative comparison of intrinsic catalytic performance. Characterization presents an additional difficulty. Ex situ XPS can identify the oxidation states present after reaction, but Co may oxidize or restructure during cooling and air exposure. Temperature-programmed techniques provide information about reducibility and adsorption strength, although they cannot directly reveal which surface structure is present during steady-state methanation. In situ DRIFTS can detect bicarbonate, carbonate, formate, methoxy, and adsorbed CO species, but the observation of an infrared band alone does not demonstrate that the corresponding species lies on the kinetically dominant reaction pathway. Combining surface-sensitive characterization with kinetic measurements is therefore necessary to distinguish active intermediates from strongly adsorbed spectators. A particularly important unresolved issue is how different oxide domains modify the competition between oxygenate-mediated and CO-mediated pathways on the same cobalt surface [15,16]. ZrO_x may preferentially stabilize bicarbonate and formate species, CeO_x may promote vacancy-assisted CO_2 activation and oxygen transfer, whereas TiO_x may exert stronger electronic and structural control over neighboring Co sites. However, these effects have rarely been evaluated using ZrO_x, CeO_x, and TiO_x domains deposited on a common Co substrate and tested

under identical reaction conditions [17,18]. Without such a controlled comparison, it remains difficult to determine whether differences in methane selectivity result from the intrinsic chemistry of the oxide–Co boundary or simply from variations in Co dispersion, reduction degree, and available metallic surface area. It is also unclear whether an oxide that improves initial CO_2 adsorption necessarily accelerates the subsequent hydrogenation steps required for CH_4 formation. Resolving this distinction is essential because strong CO_2 activation can be catalytically unproductive when intermediates accumulate faster than they can be hydrogenated.

In this study, ZrO_x-, CeO_x-, and TiO_x-decorated inverse Co catalysts are prepared using a common Co platform and evaluated for CO_2 methanation between 220 and 360°C at atmospheric pressure. The inverse architecture is used to systematically vary the chemical nature of the oxide–Co interface while minimizing differences associated with the bulk Co phase. H_2 chemisorption is employed to quantify accessible Co surface sites and distinguish intrinsic promotional effects from simple changes in metal dispersion. XPS is used to evaluate changes in Co electronic structure, interfacial charge redistribution, and resistance to oxidation induced by each oxide domain. In situ DRIFTS is applied under reaction conditions to follow the evolution of bicarbonate, carbonate, formate, adsorbed CO, and related surface intermediates and to determine how the three oxide modifiers influence their formation and consumption. By correlating normalized catalytic rates, CH_4/CO selectivity, Co surface properties, and intermediate evolution, the work aims to clarify how ZrO_x, CeO_x, and TiO_x regulate CO_2 activation and the subsequent hydrogenation sequence at inverse Co interfaces. Particular attention is given to whether improved methanation originates from increased CO_2 adsorption, accelerated conversion of oxygen-containing intermediates, stabilization of a favorable Co oxidation state, or suppression of CO desorption through more efficient interfacial hydrogenation. Establishing these relationships will provide a direct comparison of three chemically distinct oxide promoters on a common Co surface and help identify the interfacial properties that control the balance between CH_4 formation and the reverse water–gas shift pathway. More broadly, the study is intended to provide a mechanistic basis for designing inverse metal–oxide catalysts in which interfacial density and oxide chemistry can be independently tuned for efficient, selective, and low-cost CO_2 hydrogenation.

2. Materials and Methods

2.1. Catalyst Samples and Reaction Conditions

Seven catalyst samples were prepared: unmodified Co, ZrO_x/Co, CeO_x/Co, TiO_x/Co, and three physical mixtures of Co with ZrO_2, CeO_2, or TiO_2. Co particles were obtained by reducing Co_3O_4 in H_2. The inverse catalysts were prepared by depositing the oxide precursors onto the Co surface, followed by drying, mild calcination, and H_2 reduction. The oxide loading was fixed at 5 wt% for all promoted catalysts. CO_2 methanation was tested in a fixed-bed quartz reactor at atmospheric pressure. For each run, 100 mg of catalyst with a particle size of 250–425 μm was placed between two quartz-wool plugs. The feed contained CO_2, H_2, and N_2 at a volume ratio of

1:4:1. N_2 served as an internal standard. The total flow rate was 60 mL min^{-1}, giving a gas hourly space velocity of 36,000 mL g_cat^{-1} h^{-1}. The temperature was increased from 220 to 360°C in steps of 20°C. Each condition was tested three times.

2.2. Experimental Design and Control Tests

The three inverse catalysts were compared with bare Co under the same reaction conditions. This comparison was used to determine the effects of ZrO_x, CeO_x, and TiO_x on CO_2 conversion and CH_4 selectivity. Physical mixtures with the same oxide loading were also tested. These controls helped separate the effect of a close Co–oxide boundary from simple contact between separate particles. Before each reaction, the catalysts were reduced in 10 vol% H_2/N_2 at 400°C for 2 h. Blank tests were conducted without a catalyst and with oxide-only samples to check gas-phase reactions and the activity of the oxides. External mass-transfer effects were examined by changing the total flow rate from 40 to 80 mL min^{-1}. Internal diffusion was checked using catalyst particles of 150–250 and 250–425 μm. No clear change in the mass-normalized CH_4 rate was observed within these ranges.

2.3. Catalyst Characterization and Quality Control

Crystal phases were identified by X-ray diffraction with Cu Kα radiation. Particle size and oxide distribution were examined by transmission electron microscopy and energy-dispersive X-ray mapping. The surface states of Co, Zr, Ce, Ti, and O were measured by X-ray photoelectron spectroscopy. The C 1s peak at 284.8 eV was used for binding-energy correction. The exposed Co surface area was measured by H_2 chemisorption after in situ reduction. Surface species were monitored by in situ diffuse reflectance infrared Fourier-transform spectroscopy. Spectra were recorded under CO_2/H_2 flow from 220 to 360°C, and a fresh background spectrum was collected at each temperature. Reaction products were measured by online gas chromatography. CH_4 and CO were analysed with a flame-ionization detector fitted with a methanizer, while CO_2, H_2, and N_2 were measured with a thermal-conductivity detector. Calibration curves were prepared with certified standard gases. The difference between the catalyst-bed temperature and the set value was kept within ±1°C. Data were accepted when the carbon balance was between 95% and 105% and the variation among repeated tests was below 5%.

2.4. Data Processing and Calculation Methods

Gas concentrations were corrected using the N_2 internal standard. CO_2 conversion was calculated as

$$X_{CO_2}(\%) = \frac{F_{CO_2,in} - F_{CO_2,out}}{F_{CO_2,in}} \times 100,$$

where $F_{CO_2,in}$ and $F_{CO_2,out}$ are the inlet and outlet molar flow rates of CO_2, respectively. CH_4 selectivity was calculated on a carbon basis as

$$S_{CH_4}(\%) = \frac{F_{CH_4,out}}{F_{CH_4,out} + F_{CO,out}} \times 100,$$

where $F_{CH_4,out}$ and $F_{CO,out}$ are the outlet molar flow rates of CH_4 and CO, respectively. The CH_4 formation rate was calculated by dividing the outlet CH_4 molar flow by the catalyst mass. Results are reported as mean values with standard deviations. Differences among catalysts were tested by one-way analysis of variance followed by Tukey's test. A value of $p<0.05$ was considered significant.

2.5. In Situ Reaction Analysis and Stability Tests

In situ DRIFTS was used to monitor bicarbonate, carbonate, formate, adsorbed CO, and methoxy species during reaction. The catalyst was first reduced in H_2 and then exposed to the CO_2/H_2 feed at each test temperature. Spectra were collected every 2 min until no further change was observed. The band areas were compared with the CH_4 and CO formation rates to identify species linked to the main reaction pathway. Step-response tests were also carried out by switching among CO_2, H_2, and CO_2/H_2 feeds. These tests separated CO_2 adsorption from later hydrogenation steps. Catalyst stability was tested at 300°C for 40 h. After the reaction, XPS, XRD, and TEM measurements were repeated to examine Co oxidation, particle growth, and oxide movement. A catalyst was considered stable when the CH_4 formation rate changed by less than 10% and no clear phase change was detected.

3. Results and Discussion

3.1. Surface Structure and Oxide–Co Interaction

TEM and elemental mapping showed that ZrO_x, CeO_x, and TiO_x formed small domains on the Co surface. No large separate oxide particles were observed. This inverse structure created direct oxide–Co boundaries while keeping part of the Co surface open for H_2 dissociation. XPS showed shifts in the Co 2p binding energy after oxide addition, which indicates charge transfer at the interface. ZrO_x/Co showed the largest shift, suggesting a stronger electronic effect than CeO_x/Co and TiO_x/Co. H_2 chemisorption showed that oxide deposition reduced the exposed Co area. This decrease was smaller for ZrO_x/Co than for TiO_x/Co. TiO_x therefore covered more Co sites, whereas ZrO_x formed a more open interface. These structural and surface results are shown in Fig. 1. Shakil et al. (2026) also found that the activity of Co/CeO_2 depended on both exposed Co sites and the metal–oxide boundary. Their results showed that Co surface area alone could not explain the methanation rate [19,20].

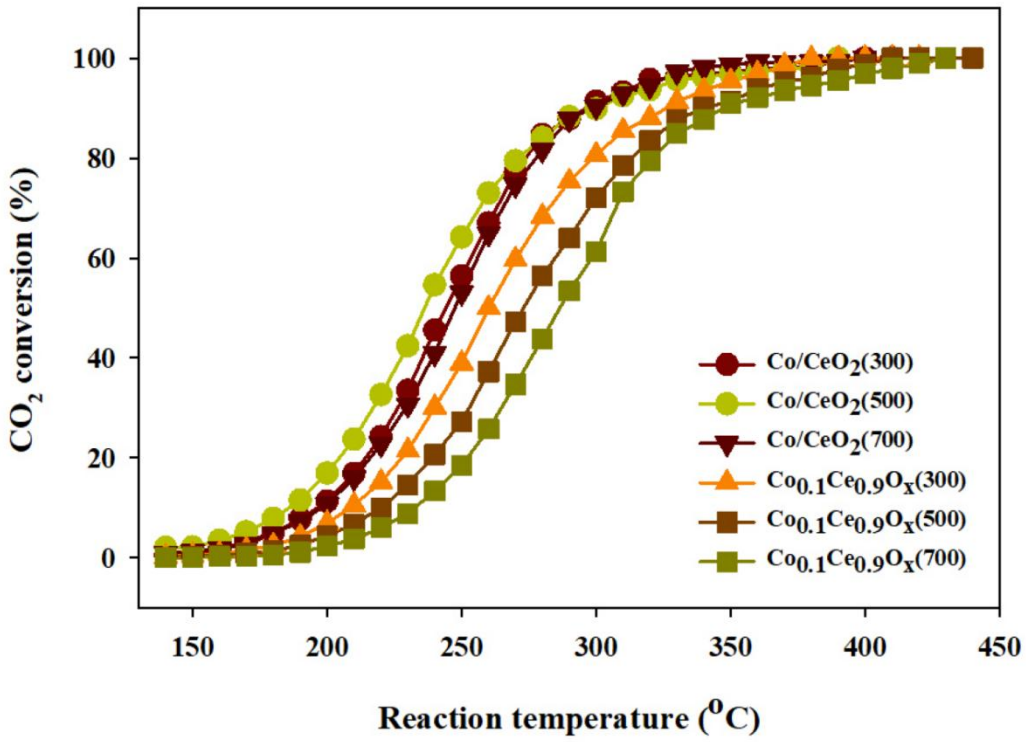

Fig. 1. Structure, surface properties, and CO_2 methanation activity of bare and oxide-modified Co catalysts.

3.2. CO_2 Conversion and CH_4 Selectivity

CO_2 conversion increased as the temperature rose from 220 to 300°C for all catalysts. Above 300°C, the increase became smaller because the methanation equilibrium became less favourable and the reverse water–gas shift reaction increased. ZrO_x/Co gave the highest activity. At 300°C, it reached a CH_4 formation rate of 7.8 mmol g_cat^{-1} h^{-1}, a CO_2 conversion of 61.4%, and a CH_4 selectivity of 96.2%, as shown in Fig. 1. The ZrO_x/Co physical mixture showed a lower rate despite having the same oxide content. This result confirms that close oxide–Co contact was needed for effective promotion. CeO_x/Co improved low-temperature conversion, but its CH_4 selectivity decreased at higher temperatures because CO formation increased. The Ce^{4+}/Ce^{3+} redox pair and oxygen vacancies promoted CO_2 activation, but strong reduction also favoured CO release. TiO_x/Co showed a smaller increase in CH_4 production. Its lower activity was related to stronger coverage of Co and fewer exposed sites for H_2 dissociation. Similar support effects have been reported for Co- and Ni-based methanation catalysts, where CeO_2, ZrO_2–CeO_2, and TiO_2 changed metal dispersion, basicity, and reaction rates in different ways [21,22].

3.3. Surface Intermediates and Reaction Pathways

In situ DRIFTS showed that the oxide promoters changed both the amount and the reaction rate of surface carbon species. Bicarbonate and formate bands appeared on all promoted catalysts after the CO_2/H_2 feed was introduced. Their changes with temperature are shown in Fig. 2. On

ZrO_x/Co, bicarbonate bands formed at low temperature and then decreased as formate bands increased. The formate signal later declined as CH_4 production increased near 300°C. This trend suggests that bicarbonate was first converted to formate and then hydrogenated to methane. The rapid loss of formate after switching to H_2 also supports its role as a reaction intermediate. On CeO_x/Co, carbonate and adsorbed CO bands remained strong at high temperature, which agrees with the higher CO content in the outlet gas. On TiO_x/Co, formate bands remained over a wider temperature range, but their slow removal suggests limited hydrogenation. Sebastian et al. (2026) also detected carbonate, bicarbonate, formate, and adsorbed CO during CO_2 methanation over Co/CeO_2. Their results showed that associative and CO-based routes can occur at the same time. Musig et al. (2026) further reported that formate, methoxy, and carbonate species changed with metal–oxide contact and support type.

3.4. Promotion Mechanism and Catalyst Stability

The results show that oxide promotion depends on more than CO_2 adsorption. A suitable promoter must activate CO_2, support hydrogen transfer from Co, and avoid excessive coverage of metallic Co sites. ZrO_x provided the best balance among these effects. Its acid–base oxygen sites promoted bicarbonate and formate formation. The open ZrO_x–Co boundary also allowed rapid hydrogen transfer and further C–O bond removal. CeO_x provided more oxygen-storage sites, but its redox activity increased the CO pathway at high temperature. TiO_x formed strong contact with Co, but its greater surface coverage reduced the number of H_2 activation sites. During the 40 h test at 300°C, ZrO_x/Co showed only a small decrease in CH_4 production. Post-reaction XPS also showed less Co oxidation than on bare Co. The ZrO_x promoter therefore helped maintain a reduced Co surface in the presence of reaction water. The proposed interface reactions and stability results are shown in Fig. 2. However, the tests were conducted at atmospheric pressure and with one oxide loading. Longer tests, different oxide contents, and operando measurements of the Co oxidation state are still needed under higher-pressure conditions [23,24].

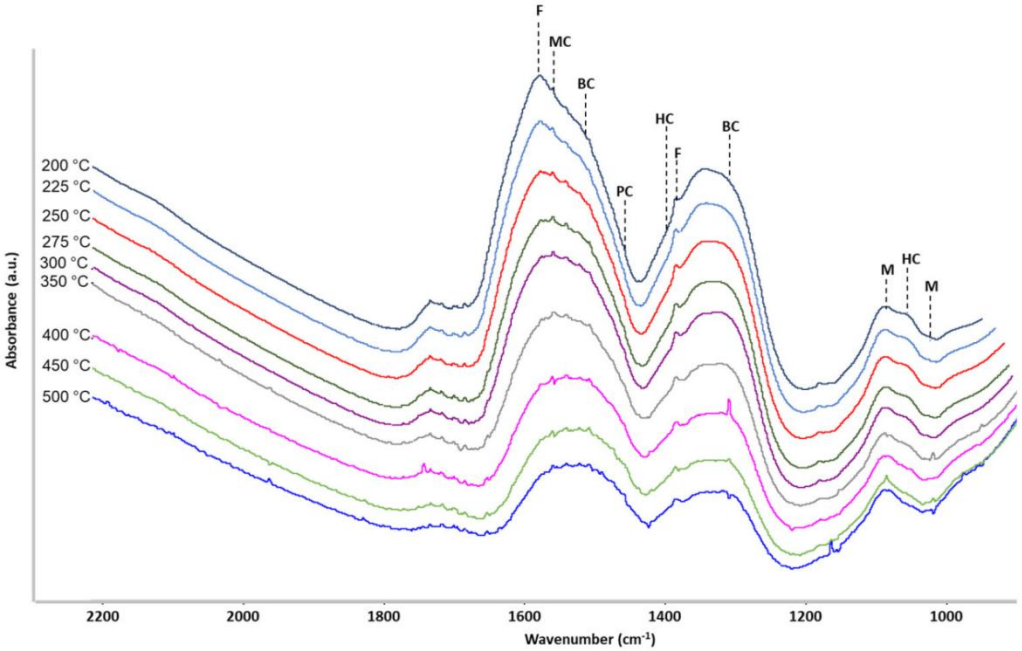

Fig. 2. Surface species, catalyst stability, and CO_2 methanation routes at oxide–Co interfaces.

4. Conclusion

Inverse oxide modification changed CO_2 activation and hydrogenation on Co catalysts. ZrO_x/Co showed the best performance, with a CH_4 formation rate of 7.8 mmol g_cat^{-1} h^{-1}, a CO_2 conversion of 61.4%, and a CH_4 selectivity of 96.2% at 300°C. The ZrO_x–Co interface promoted the formation of bicarbonate and formate species and supported their further hydrogenation to CH_4. CeO_x improved CO_2 adsorption and oxygen transfer but increased CO formation at higher temperatures. TiO_x interacted strongly with Co, but partial coverage of metallic Co reduced H_2 activation. ZrO_x also helped keep Co in a reduced state during the 40 h stability test. This study directly compared three inverse oxide promoters at the same loading and under the same reaction conditions. The results show that an effective promoter should improve CO_2 adsorption, support hydrogen transfer, and retain enough metallic Co sites. This method may help develop Co-based catalysts for low-temperature CH_4 production. However, the tests were conducted at atmospheric pressure with one oxide loading. Further studies should examine different promoter amounts, longer reaction times, higher pressures, and operando measurements of the Co oxidation state.

References

1. Chen, F., Liang, H., Li, S., Yue, L., & Xu, P. (2025). Design of Domestic Chip Scheduling Architecture for Smart Grid Based on Edge Collaboration.

2. Kwak, M., Park, G. H., Ha, J., Choi, S., Kim, S., Heo, J., ... & Kim, W. B. (2026). Phase-reconstructed exsolution strategy of metal catalysts on Ruddlesden-Popper perovskites to drive highly rapid polysulfide conversion in lithium-sulfur batteries. Journal of Energy Chemistry.

3. Yang, Z., Alexandrova, A. N., & Sautet, P. (2026). Modeling CO2 Hydrogenation to Methanol on an Ensemble of Inverse ZrO2 on Cu Catalytic Sites: Mechanism, Reactivity, and Deactivation. Angewandte Chemie, e5448247.

4. Kiss, J., Szenti, I., Efremova, A., Kovács, I., Deér, A., Sápi, A., & Kónya, Z. (2026). Surface Intermediates in Important Catalytic Reactions: Formation, Identification and Reactivity Across Metals, Nanoparticles and Supported Catalysts. Catalysts, 16(5), 404.

5. Liang, R., Feifan, F. N. U., Liang, Y., & Ye, Z. (2025). Emotion-Aware Interface Adaptation in Mobile Applications Based on Color Psychology and Multimodal User State Recognition. Frontiers in Artificial Intelligence Research, 2(1), 51-57.

6. Stamatelos, I., Guo, Z., Pasel, J., & Saei, W. (2026). Oxide-derived metals and alloys: from dynamic reconstruction to function across electrocatalytic reactions. Energy Advances.

7. Liang, S., Zhang, X., Du, Y., & Chen, W. (2026). Supply Network Restructuring and Capacity Ramp-Up Limits in the Localized Expansion of High-Performance Computing Equipment Production. Available at SSRN 7339738.

8. Bao, Y., & Wang, H. (2026). Edge-to-Cloud Infrastructure Continuum: A Unified Framework for Optimizing Industrial IoT Systems. Available at SSRN 7185578.

9. Nasim, F., & Nadeem, M. A. (2025). Decoding d-Band Effects: Impact of Diverse Environments on Cobalt's Catalytic Performance in Oxygen Reduction Reaction. ChemCatChem, 17(14), e00437.

10. Du, Y. (2025). Research on Digital Quality Traceability System for Temperature-Controlled Supply Chain of Foreign Trade Wine Driven by Blockchain and IoT. Business and Social Sciences Proceedings, 4, 57-65.

11. Jiao, Y., Zhao, B., Wang, A., & Shi, T. (2026). Construction and Empirical Study of a Modularized Teaching System for Art Courses Based on a Unified Training Pathway.

12. Sebastian, J., Mebrahtu, C., Zeng, F., & Palkovits, R. (2026). Strong Metal-Support Interactions on TiO2-Supported Metal Catalysts for Fine-Tuning Catalysis. Angewandte Chemie International Edition, 65(1), e02611.

13. Yang, J. (2026). Stage-Coupled Computational Framework for Stratified Accessibility and Equity Analysis in Community-Based Elderly Care Services.

14. Prabhakar Reddy, K., Lim, H., Islam, A., Tian, Y., Hunt, A., Waluyo, I., & Rodriguez, J. A. (2025). CO2 Adsorption and Hydrogenation on Inverse InO x/Cu (111) Catalysts: Active Role of the Oxide–Metal Interface. ACS Applied Materials & Interfaces, 17(25), 36810-36820.

15. Wu, J., Wu, D., Zhang, J., & Peng, Y. (2026). Generative AI Feedback in Junior High School Artistic Creation Evaluation. Available at SSRN 7244838.

16. Shakil, R., Akhe, A. S., Wahid, F., Imran, A. B., & Chowdhury, A. N. (2026). Carbon-based Solar Fuels: Methanol, Ethanol, and Beyond. Solar Fuels: Technologies and Applications for a Sustainable Energy Future, 1, 289-324.

17. Gu, X. (2026). Identifying Causal Effects and Analyzing Heterogeneity of User Growth Interventions on Digital Platforms: Evidence from Large-Scale Behavioral Data. Available at SSRN 6809181.
18. Pozzati, M., Deriu, C., Ragonese, P., Cattelan, M., Lamberti, F., Zahorodna, V., ... & Wang, M. (2026). MXene-modified BiVO4/FePO4 photoanodes for solar oxygen evolution. Nanoscale Advances.
19. Villardon, A., Gallego-Mena, L., Dorado, F., & Sanchez-Silva, L. (2026). Olive stone-derived hydrochars for CO2 methanation: synergistic and antagonistic effects of ZnCl2 and FeCl2 in Ni-based catalysts. Energy Conversion and Management: X, 101851.
20. Bao, Y., Qiu, Y., & Wang, H. (2026, May). Unified Identity Layer for Hyperscale Ecosystems: A Framework for Cross-Platform User Attribution and Experimentation. In 2026 6th International Conference on Machine Learning and Intelligent Systems Engineering (MLISE) (pp. 540-543). IEEE.
21. Musig, B., Aznar, M., Gálvez, M. E., & Navarro, M. V. (2026). CeO2-Based and Containing Catalysts for CO2 Methanation: A Short Review.
22. You, S. (2026). Verifiable Audit Mechanisms in AI Compliance Automation: Scalability. Available at SSRN 6547458.
23. Jiao, Y., Shi, T., Zhao, B., & Wang, A. (2026). The Impact of VR Sketching Simulations on the Assessment of Scale and Site Suitability in Public Art Spaces.
24. van den Bosch, I. C., Zaman, J. U., Shterk, G., Hamed, M. H., Schneider, M., Ratovskii, V., ... & Baeumer, C. (2025). Laboratory-based in situ and operando tricolor x-ray photoelectron spectroscopy. Science advances, 11(34), eadw6673.